CANCER

Switching the intracellular pathway and enhancing the therapeutic efficacy of small interfering RNA by auroliposome

Md. Nazir Hossen[1,2], Lin Wang[3], Harisha R. Chinthalapally[1,2], Joe D. Robertson[4], Kar-Ming Fung[1,2], Stefan Wilhelm[5], Magdalena Bieniasz[3], Resham Bhattacharya[6], Priyabrata Mukherjee[1,2]*

Gene silencing using small-interfering RNA (siRNA) is a viable therapeutic approach; however, the lack of effective delivery systems limits its clinical translation. Herein, we doped conventional siRNA-liposomal formulations with gold nanoparticles to create "auroliposomes," which significantly enhanced gene silencing. We targeted MICU1, a novel glycolytic switch in ovarian cancer, and delivered MICU1-siRNA using three delivery systems—commercial transfection agents, conventional liposomes, and auroliposomes. Low-dose siRNA via transfection or conventional liposomes was ineffective for MICU1 silencing; however, in auroliposomes, the same dose gave >85% gene silencing. Efficacy was evident from both in vitro growth assays of ovarian cancer cells and in vivo tumor growth in human ovarian cell line—and patient-derived xenograft models. Incorporation of gold nanoparticles shifted intracellular uptake pathways such that liposomes avoided degradation within lysosomes. Auroliposomes were nontoxic to vital organs. Therefore, auroliposomes represent a novel siRNA delivery system with superior efficacy for multiple therapeutic applications.

INTRODUCTION

The therapeutic potential of sequence-specific gene knockdown by small interfering RNAs (siRNAs) was demonstrated over 20 years ago (*1*–*2*). However, the lack of effective and nontoxic delivery systems has limited their clinical progress. Ineffective delivery is compounded by specific siRNA properties, including high molecular weight, anionic charge, hydrophilicity, and potential for degradation by nucleases; these properties limit the ability of siRNAs to cross negatively charged plasma membranes and survive intracellularly without degradation in lysosome for prolonged periods. Facilitating siRNA delivery and promoting endosomal and/or lysosomal escape are essential for effective gene silencing (*3*). Liposomal formulations overcome some of these challenges and remain the most widely used strategy for siRNA delivery (*4*); ease of formulation and the tunability of critical parameters such as size, charge, siRNA loading, and circulation time make liposomes an attractive choice (*5*–*7*).

The first U.S. Food and Drug Administration (FDA)–approved liposomal drug was Doxil, a formulation of doxorubicin approved in 1995 for treatment of AIDS-related Kaposi's sarcoma; approval was later expanded to ovarian cancer (*8*–*10*). Since then, multiple liposomal formulations have been approved including both chemotherapeutics and vaccines (*8*–*10*); others are in phase 2 and 3 clinical trials for multiple malignancies (*10*). In contrast, clinical translation of siRNA-based therapies remains rare; in 2018, the lipid nanoparticle-based siRNA (Patisiran) was FDA-approved for the treatment of polyneuropathy (*11*). Several liposomal siRNA formulations are in phase 1 clinical trials, including treatments for pancreatic cancer (PKN3 siRNA), liver cancer (CEBPA siRNA), and neuroendocrine tumors (PLK1 siRNA) (*10*). While liposomes are an established method for drug delivery, their potential for siRNA delivery has not been fully realized.

Here, we report the development of a novel siRNA-liposomal formulation; we demonstrate that incorporation of 20-nm gold nanoparticles (AuNPs) in a liposomal formulation modulates both the intracellular uptake pathway and silencing efficacy. We also show that our novel "auroliposome" formulation both enhances tumor suppression in vivo and lacks significant toxicity compared to conventional liposomes (cLPs).

RESULTS

Optimization of physicochemical parameters and chemical compositions for effective gene silencing in vitro

We initially identified a liposomal formulation that optimally delivered cystathionine β-synthase (CBS)—siRNA to cancer cells; CBS was selected as the model target since we previously showed that liposomal CBS-siRNA inhibits tumor growth and metastasis in human xenograft models of ovarian cancer (*12*). We created a library of 11 liposomes by varying the ratios of several commonly used ingredients (fig. S1, A to C); incorporated ingredients were DOTAP (1,2-dioleoyl-3-trimethylammonium-propane), DOPE (1,2-dioleoyl-*sn*-glycero-3-phosphoethanolamine), DOPC (1,2-dioleoyl-*sn*-glycero-3-phosphocholine), PE-PEG (1,2-dioleoyl-*sn*-glycero-3-phosphoethanolamine-*N*-[methoxy (polyethylene glycol 2000)] ammonium salt), and CBS-siRNA. DOTAP has a positive charge, DOPE is neutral, and PE-PEG, DOPC, and siRNA are negatively charged; in addition to modulating the charge of liposomes, PE-PEG also prolongs circulation time through the stealth property it imparts. Low-level Tween 20, a cellular pore-forming surfactant, was incorporated to facilitate uptake of liposomes (fig. S1, A and B) (*5*).

[1]Peggy and Charles Stephenson Cancer Center, University of Oklahoma Health Science Center, Oklahoma City, OK 73104, USA. [2]Department of Pathology, University of Oklahoma Health Science Center, Oklahoma City, OK 73104, USA. [3]Aging and Metabolism Research Program, Oklahoma Medical Research Foundation, Oklahoma City, OK 73104, USA. [4]Department of Chemistry and University of Missouri Research Reactor, University of Missouri, Columbia, MO 65211, USA. [5]Stephenson School of Biomedical Engineering, University of Oklahoma, Norman, OK 73072, USA. [6]Department of Obstetrics and Gynecology, University of Oklahoma Health Science Center, Oklahoma City, OK 73104, USA.
*Corresponding author. Email: priyabrata-mukherjee@ouhsc.edu

One liposomal formulation contained no siRNA and was designated empty liposomes (E-LPs); the remaining 10, designated F1-F10, all contained siRNA as specified (fig. S1C). These liposomes were physicochemically characterized by dynamic light scattering (DLS), zeta potential measurements, transmission electron microscopy (TEM), and RiboGreen assay. All formulations had hydrodynamic diameters, determined by DLS, of ~130 nm (fig. S1D, top). In terms of charge, the E-LPs, composed of 50:50 (w/w) DOTAP:DOPE, were at ~+50 mV; decreasing DOTAP or incorporating other components, DOPC, PE-PEG, or siRNA, reduced the charge of all liposomes (fig. S1D, bottom). We used the RiboGreen assay to quantify incorporated siRNA and all liposomes exhibited siRNA encapsulation efficiencies of ~90% (fig. S1E).

Having characterized the liposomes, we tested the efficacy of each formulation to down-regulate CBS in ovarian cancer cells. Preliminary experiments determined an appropriate siRNA dose; increasing doses of CBS-siRNA were transfected into cells using HiPerFect (HF). Western blot analyses showed ~30% reduction in CBS protein with 25 nM CBS-siRNA and ~80% reduction at 133 nM (Fig. 1A). Since we expected siRNA liposomes to enhance the silencing effect, we incorporated 25 nM CBS-siRNA in our liposomes (F1-F10) and compared their silencing efficacy with 25 and 133 nM CBS-siRNA administered using HF. At 25 nM, only F7 significantly down-regulated CBS protein (~65%); this level of CBS down-regulation was comparable to that with 133 nM CBS-siRNA delivered using HF (Fig. 1B). Thus, we selected the F7 formulation for further study; F7 was designated the cLP.

For effective siRNA delivery, the liposomes surface charge is critically important; it affects multiple determinants of efficacy including cellular uptake, endosomal escape, biostability, and tumor penetration. Compared to cationic and anionic liposomes, neutral liposomes are relatively biostable, recognized less by the reticuloendothelial system (RES), and penetrate tumors better (*6*, *13*). However, neutral liposomes also have diminished cellular uptake necessitating additional design considerations to ensure effective siRNA delivery; reports demonstrating the effective use of neutral DOPC-based siRNA liposomes to reduce expression of a target in vivo are rare (*5*).

Although F7 was our most efficacious formulation in vitro, it is a positively charged particle (fig. S1D) and thus likely to be rapidly cleared in vivo. To enhance in vivo effectiveness, we aimed to reduce the positive charge of F7 by replacing the aqueous solution of siRNA with an aqueous solution containing a mixture of AuNPs and siRNA; citrate-capped AuNPs have a net negative charge of ~−40 mV. AuNPs provide additional potential benefits; they are biocompatible, have self-therapeutic properties, and, when necessary, are easily surface functionalized (*14*, *15*). Among different sized AuNPs, those of 20 nm are the best inhibitors of angiogenesis and tumor growth (*15*). We incorporated 20-nm AuNP in our F7 formulation; hereafter F7 liposomes containing 20-nm AuNP are termed auroliposomes (AuroLPs) (Fig. 1C). We characterized auroLPs with three different siRNA:AuNP w:w ratios, 1:5, 1:10, and 1:20, using DLS, zeta potential, TEM, and RiboGreen. auroLP sizes did not differ appreciably from F7 (Fig. 1D). However, auroLP charge was significantly lower than F7; charges were ~+40 mV for F7 and ~+14, +10, and +9 mV for the 1:5, 1:10, and 1:20 ratio auroLPs, respectively (Fig. 1E). In addition, siRNA encapsulation efficiency was unaffected by incorporation of AuNPs (Fig. 1F). The stability of auroLPs was assessed by treatment with 150 mM NaCl (final salt concentration); dilute NaCl solutions aggregate any nonstabilized AuNP causing precipitation (*16*). auroLPs of the siRNA:AuNP 1:5 ratio had a reddish purple color; this color intensified at the 1:10 ratio indicating increased AuNP incorporation (fig. S1F). The color changed to black when the ratio increased to 1:20, indicating aggregation of AuNPs (*17*). When treated with 150 mM NaCl, the color of 1:10 ratio extruded liposomes persisted; similar treatment of the 1:5 and 1:20 ratio auroLPs caused the color to disappear indicating aggregation (fig. S1F). To further support that AuNP are indeed encapsulated within the liposome at our optimized ratio of 1:10 siRNA:AuNP, we performed the same studies using 150 mM NaCl and measured the optical density of the resulting solution. The presence of a surface plasmon resonance (SPR) band at 521 nm is indicative of the formation of AuNP of ~20 nm by the citrate reduction method (*15*). Disappearance of this band following addition of 150 mM NaCl accompanied by the appearance of black precipitate confirms aggregation of AuNPs (fig. S2A) (*16*). In addition, the 521-nm SPR band of AuNPs is red-shifted to 550 nm when mixed with cLPs, indicating binding of AuNPs by the cLPs. However, as with as-synthesized AuNPs, when this mixture was treated with NaCl, the SPR band of AuNP disappeared, confirming aggregation of cLP surface bound AuNPs (fig. S2B) (*18*). The SPR band of AuNP in auroLP was retained, although with some dampening of the absorbance, on treatment with NaCl, confirming enhanced stability and encapsulation of AuNPs in auroLPs (fig. S2C). TEM images showed that both NaCl-treated and NaCl-untreated auroLPs had similar morphology (fig. S2F). TEM micrographs showed the typical "currant bun" like morphology of liposomes, with AuNPs distributed throughout the core and at the surface, along with irregular water filled cavities inside the lipid bilayer (fig. S2D), consistent with previous reports (*18*–*20*). We also counted the number of AuNPs visible in TEMs of auroLPs with different siRNA:AuNP ratios. Most auroLPs at siRNA:AuNP ratio of 1:10 contained three to six AuNPs, whereas at the 1:5 and 1:20 ratios, liposomes contained one to two AuNPs each (fig. S2E). Quantification of gold content by instrumental neutron activation analysis (INAA) also suggested that AuNP incorporation increased between the 1:5 and 1:10 ratios (~2% incorporation of the dosed AuNP) but decreased at the 1:20 ratio (~1% incorporation) possibly due to the aggregation discussed above (Fig. 1G). Together, ultraviolet-visible (UV-vis) and TEM studies confirm that most of the AuNPs are distributed throughout the core of the auroLP, although we cannot rule out the possibility that AuNPs are also present at the surface of auroLP.

We also assessed the ability of our novel auroLPs to down-regulate CBS in CP20 ovarian cancer cells; we used the 25 nM siRNA dose and compared auroLPs with cLP and HF. auroLPs with the siRNA:AuNP ratio of 1:10 were the most effective of all approaches with ~95% down-regulation (Fig. 1H). Control cLPs containing scrambled siRNAs and auroLPs with or without scrambled siRNA, CBS-siRNA-AuNP, and CBS-siRNA-AuNP + cLPs had no effect on CBS; it was AuNP incorporation that enhanced efficacy of siRNA (Fig. 1, H and I, and fig. S3, A and B). In addition to better understand roles of AuNP in liposomal formulation, we used two additional groups: (i) First, pretreated cells with the same amount of AuNP as in AuroLPs for 2 hours followed by treatment with CBS-siRNA-cLPs; (ii) a mixture of CBS-siRNA-cLPs and same amount of AuNP as present in AuroLPs. These treatment groups demonstrated same efficacy in gene silencing as cLPs as observed in reduction of CBS protein expression (Fig. 1I), further suggesting that encapsulation of AuNP is essential for enhanced efficacy observed in AuroLPs. We confirmed the impact of auroLPs (1:10) in a second ovarian cancer

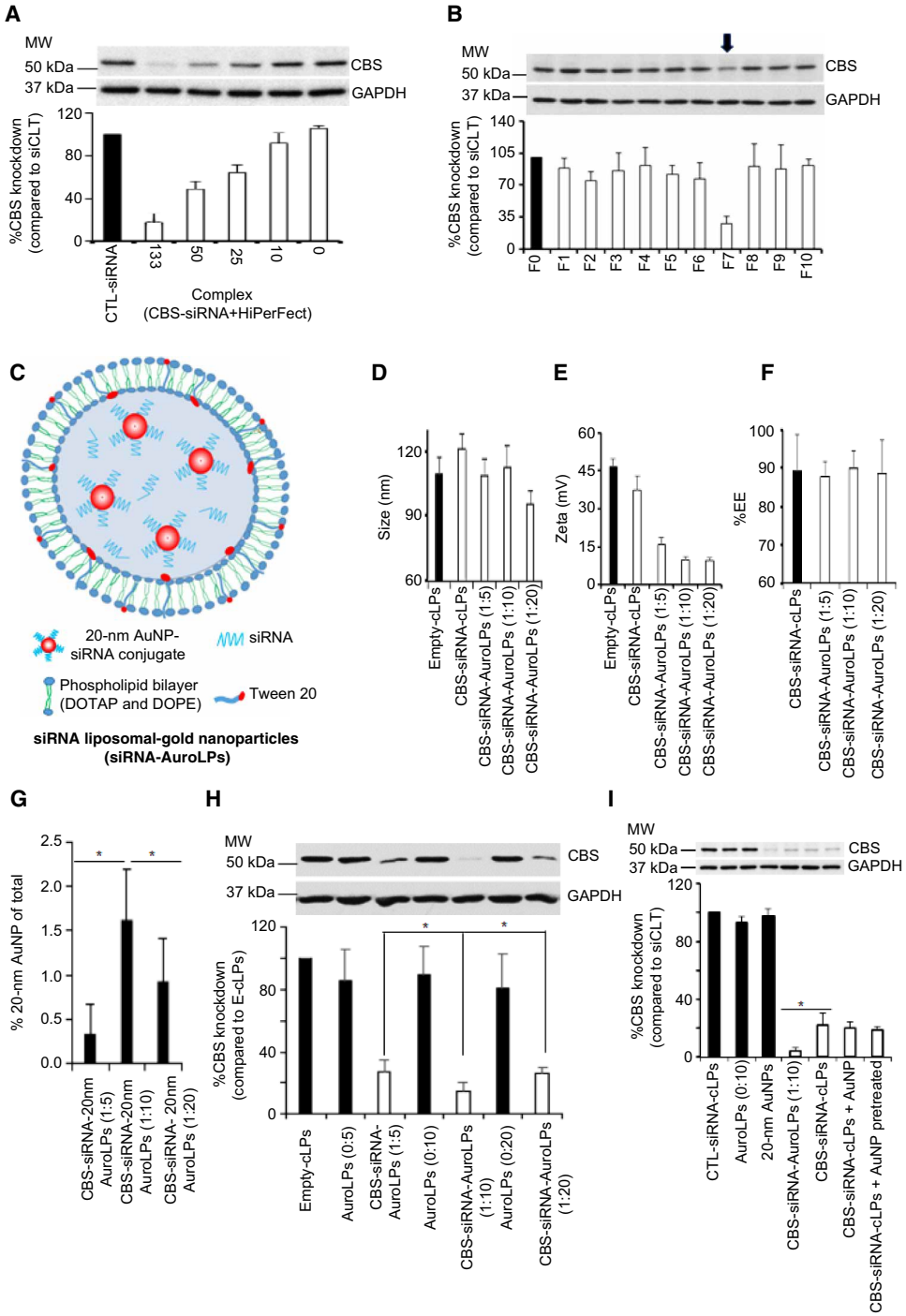

Fig. 1. Physicochemical characterization of liposomal formulation. (**A**) CP20 cells were transfected with difference concentrations of CBS-siRNA or control siRNA using HF transfection reagent for 48 hours; CBS silencing was determined by Western blot (WB). (**B**) Liposome screening: CP20 were treated with CBS-siRNA-LPs (F1-F10) or control (CTL)–siRNA-LPs (F0) for 48 hours; CBS silencing was determined by WB. (**C**) Schematic representation of siRNA-AuroLPs. (**D** and **E**) The size and charge of liposomal formulation with/without CBS-siRNA were measured by Zetasizer. (**F**) Entrapment of CBS-siRNA into AuroLPs. (**G**) AuNP content in cLPs analyzed by INAA. (**H**) Gene silencing efficacy by AuroLPs having various CBS-siRNA/20-nm AuNP ratio (w/w); silencing was determined by WB 48 hours after treatment. (**I**) Silencing efficacy by AuroLPs. Cells were treated with different groups for 48 hours; CBS silencing was determined by WB. Data are represented as means ± SD, *$P < 0.05$, $n = 3$, with Student's t test. ImageJ was used for intensity quantitation of CBS protein, normalized by glyceraldehyde-3-phosphate dehydrogenase (GAPDH) as loading control.

cell line OVCAR4 (fig. S3B); transient down-regulation of CBS could be observed up to 4 days (fig. S3C).

We additionally assessed whether our auroLPs affected cellular viability and clonal growth in two ovarian cancer cell lines, OV90 and OVCAR4. auroLPs (1:10) significantly reduced viability and clonal growth in both cell types and did so more effectively than cLPs or HF-delivered siRNA (fig. S3, D and E).

Thus, 20-nm AuNPs incorporated into conventional siRNA liposomes at a siRNA:AuNP ratio of 1:10 enhance the efficacy of siRNA to down-regulate the model target protein. Having shown this, we investigated whether the size, shape, or material comprising the nanoparticle was important.

Effect of nanoparticle size, shape, and core material in silencing efficacy of AuroLPs

For the following studies to investigate the impact of nanoparticle size, shape, or core material, we changed our molecular target to mitochondrial calcium uptake 1 (MICU1); we chose to target MICU1 since we recently demonstrated that it is a glycolytic switch in ovarian cancer that promotes both tumor growth and therapy resistance (*21*) and no small-molecule inhibitor of MICU1 has been identified. Validation of MICU1 silencing using our formulation could lead to future clinical translation of novel MICU1-targeted therapies for ovarian cancer.

To assess size effects, we selected spherical AuNPs of 5, 20, and 50 nm; for shape and core material comparisons, we used 25-nm gold nanorods (GNRs) and 20-nm iron oxide nanoparticles (Fe_3O_4NP), respectively. DLS showed that all liposomes were ~120 nm in size, except those containing 50-nm AuNPs which were ~150 nm (fig. S4). Incorporation of Fe_3O_4NPs decreased the charge of liposomes from ~+50 to ~−6 mV, the 5- and 50-nm AuNPs reduced the charge to ~+37 mV, and both the 20-nm AuNPs and 25-nm GNR reduced the charge to ~+8 mV (fig. S4). Moreover, sizes were also confirmed by TEM (fig. S5, A and B). The encapsulation efficiency of MICU1-siRNA was ~90% for all spherical AuNPs but significantly less for both GNR and Fe_3O_4NPs (fig. S4). Next, we determined knockdown of MICU1 in vitro using liposomes containing each nanoparticle at siRNA:AuNP ratios of 1:10; only liposomes containing AuNPs caused significant MICU1 knockdown with 20-nm AuNP being the best (Fig. 2, A to C). To confirm that decreased MICU1 protein resulted from transcriptional down-regulation, we determined MICU1 mRNA levels; MICU1-siRNA auroLPs significantly reduced MICU1 mRNA levels compared to either MICU1-siRNA-cLPs or MICU1-siRNA delivered by HF (Fig. 2D). We compared auroLPs containing 25 nM MICU1-siRNA to the same dose delivered by two other commercially available transfection agents (Lipofectamine 3000 and RNA iMax); auroLPs were superior to both (Fig. 2E). Together, these data show that size, shape, and core material of incorporated nanoparticles are critical to down-regulation of target proteins by liposomal siRNA. Although we identified 20-nm circular AuNPs as optimal to enhance siRNA efficacy, the underlying mechanism(s) of enhancement is unclear.

Having identified the best auroLP formulation, we thoroughly characterized this final formulation in vitro. Size, charge, and siRNA encapsulation efficiency were similar to those discussed above. We determined serum stability by incubation in fetal bovine serum (FBS) followed by agarose gel electrophoresis; at 96-hour incubation, MICU1-siRNA in auroLPs was stable, whereas it started to release from cLPs at that time point and was completely degraded in all controls (Fig. 2F). The release kinetics of siRNA from liposomes was also assessed; ~12% MICU1-siRNA was released from auroLPs compared to ~6% release from either cLPs or HF in an endo-/lysosomal environment, i.e., pH 5.0 and 10 mM glutathione (GSH) for 24 hours (fig. S6A). Last, MICU1 auroLPs more effectively reduced clonal growth (~90%) of ovarian cancer cells than any other treatment. (Fig. 2G and fig. S6B). These collective data confirm that MICU1-siRNA in our liposome is stable and efficiently down-regulates MICU1 levels, leading to robust inhibition of clonal growth of ovarian cancer cells.

Comparison of biodistribution, toxicity, and therapeutic efficacy of MICU1-siRNA between cLPs and auroLPs

We assessed the therapeutic efficacy of MICU1-siRNA auroLPs in a human xenograft model of ovarian cancer generated by subcutaneous implantation of OV90 cells. First, we determined liposome biodistribution; once implanted tumors reached ~500 mm^3, animals were intravenously injected with 5 μg of Cy5 labeled control (CTL) siRNA in either cLPs or AuroLPs. Twenty-four hours later, ~8% of injected auroLPs had accumulated in tumor tissue, almost twice the level of cLPs (Fig. 3, A and B). The lower accumulation of cLPs is due to the highly positive surface charge that favors complement activation and macrophage uptake in blood, leading to a decreased stability in the systemic circulation and subsequently reduced accumulation in the tumor site (*6*, *7*, *13*). In contrast, emerging evidence shows that neutral liposomes (such as AuroLPs) do not cause complement activation, evade recognition by macrophages, have increased retention in the blood and thus higher accumulation in tumor (*6*, *7*, *13*). The uptake mechanism of both liposomal formulations was mediated by the enhanced permeability and retention (EPR) effect exploiting the leaky, tortuous, and highly permeable tumor vasculature (*22*). Uptake is inversely proportional to the charge of the nanosystems. Together, this evidence suggests that the enhanced accumulation of AuroLPs via the EPR effect in the tumor is due to its reduced surface charge as compared to the highly cationic cLPs. Next, we assessed therapeutic response. When implanted tumors reached ~100 mm^3, we initiated treatment by intravenous injection of 0.2-mg siRNA/kg body weight; treatments were either control siRNA or MICU1-siRNA packaged in either cLPs or auroLPs given every 4 days for 12 days. The auroLPs reduced tumor growth significantly more than either cLP or control treatments; auroLPs reduced tumor ~80% compared to <50% for cLPs (Fig. 3, C to E). We also probed expression of MICU1 in tumor tissues at both the mRNA and protein levels; auroLPs caused robust down-regulation of both (Fig. 3, F and G). Immunohistochemical staining confirmed auroLP-mediated reductions of MICU1 levels (Fig. 3H). Inhibition of tumor growth was also shown by staining for a decrease in proliferating cells (Ki67 staining) and an increase in apoptotic cells [TUNEL (terminal deoxynucleotidyl transferase–mediated deoxyuridine triphosphate nick end labeling) staining] (Fig. 3, I and J); hematoxylin and eosin (H&E) staining revealed lower density of tumor cells and an increased in pyknotic nuclei in the auroLP-treated group than the other groups. H&E staining of liver, spleen, lungs, kidneys, and heart demonstrated the absence of toxicity from auroLP treatment; cLPs caused slight toxic effects in liver (hepatitis) and lungs (accumulation of inflammatory cells) (Fig. 3K and fig. S7A). In general, following intravenous injection, most of liposomes are rapidly cleared from blood by two major mechanisms: (i) Drug leakage through destabilization of the lipid membrane of liposomes due to association with high- and low-density lipoproteins or activation of

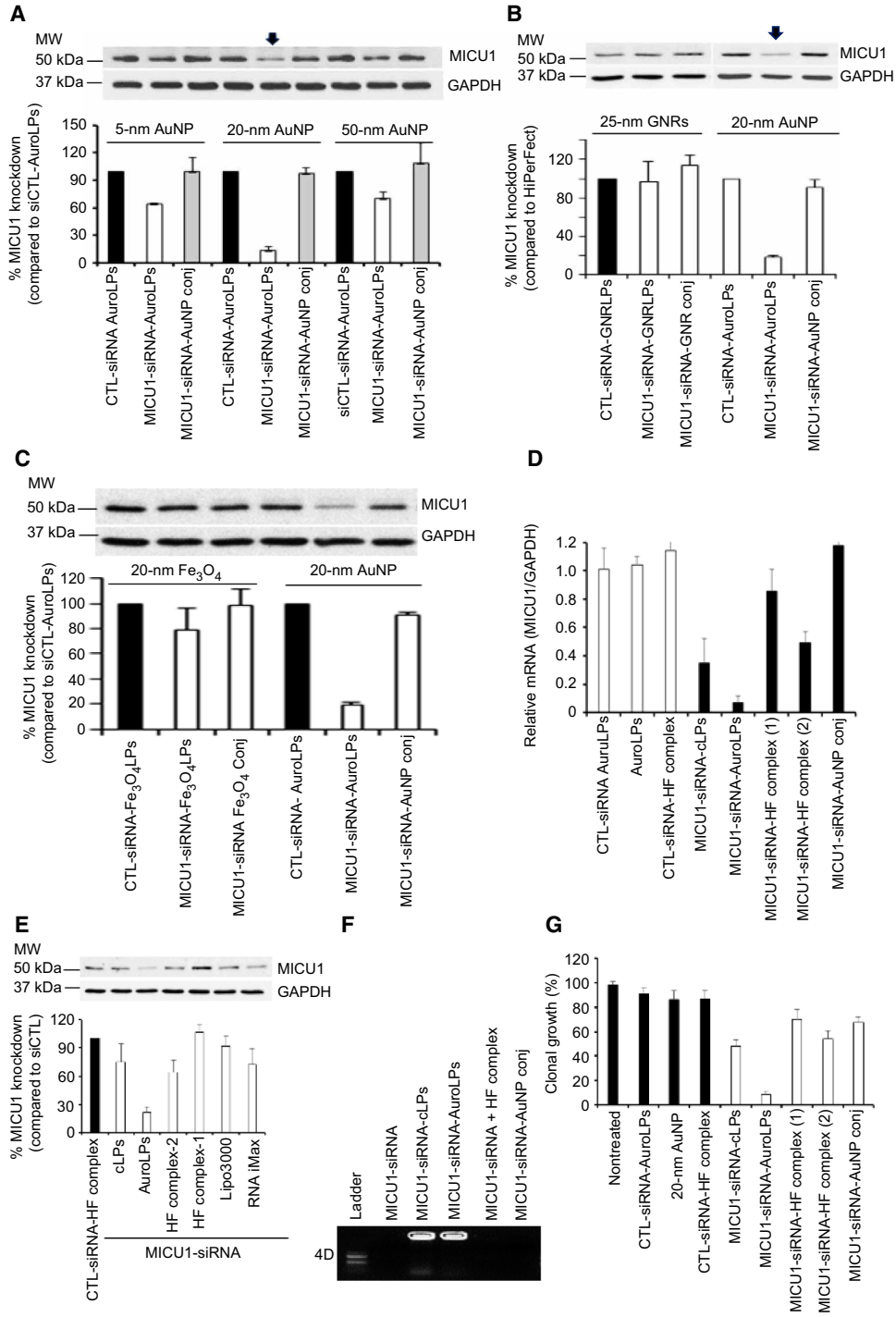

Fig. 2. Effect of nanoparticle size, shape, and core material in gene silencing efficacy AuroLPs. (**A** to **C**) WB demonstrating effect on MICU1 protein expression by treatment with nanoparticles of different sizes, shapes, and core materials containing MICU1-siRNA entrapped in traditional liposome or along with inorganic nanoparticles. (C) MICU1-siRNA-20 nm Fe_3O_4LPs effect on MICU1 protein expression as observed by WB. (**D**) Analysis of MICU1 silencing at the mRNA level by quantitative real-time polymerase chain reaction (qRT-PCR) via the treatment of cells with CTL-siRNA-AuroLPs, 20-nm AuNP, CTL-siRNA-HF, MICU1-siRNA-AuroLPs, MICU1-siRNA-cLPs, complex (1) (25 nM) or complex (2) (100 nM), and MICU1-siRNA-20 nm AuNP. (**E**) WB analysis demonstrating silencing efficacy of MICU1-siRNA in CTL-siRNA-HF complex (100 nM), complex (1) and complex-2 or MICU1-siRNA-cLPs, MICU1-siRNA-AuroLPs, MICU1-siRNA-Lipofectamine 3000, and MICU1-siRNA-RNAiMax complex (25 nM) by treating the cells for 72 hours. (**F**) Stability of MICU1-siRNA, MICU1-siRNA-cLPs, MICU1-siRNA-AuroLPs, MICU1-siRNA-HF complex, and MICU1-siRNA-20 nm AuNP for 96 hours by electrophoresis. (**G**) Inhibition of clonal growth by treatment with CTL-siRNA-AuroLPs, 20-nm AuNP, CTL-siRNA complex, MICU1-siRNA-AuroLPs, MICU1-siRNA-cLPs, complex (1) or complex (2), and conjugate (25 nM) for 12-day through crystal violet staining. Data were expressed as means ± SD. ImageJ was used for quantitation of MICU1 protein, normalized by GAPDH as loading control.

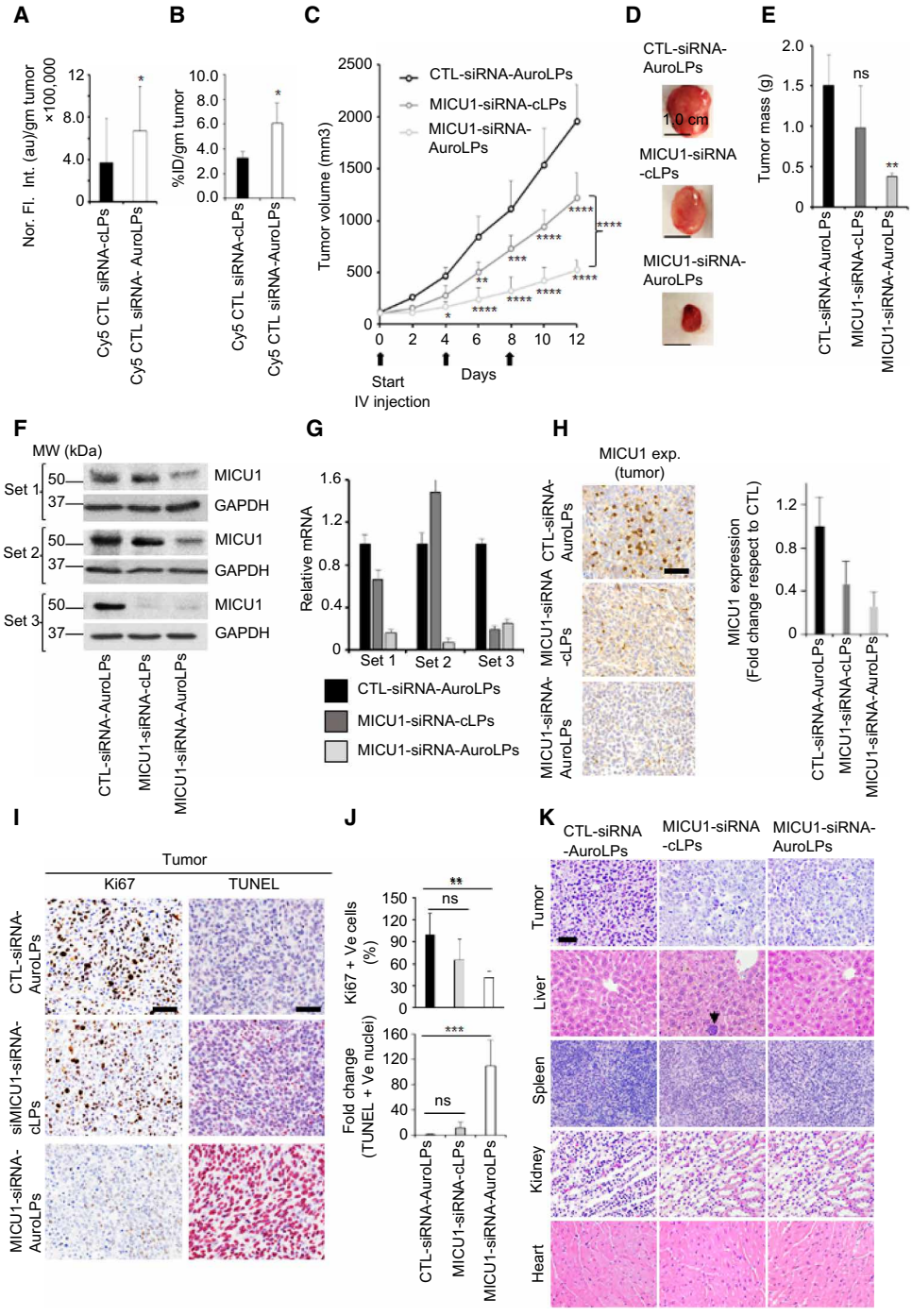

Fig. 3. Tumor accumulation of AuroLPs and its effect on tumor growth. (**A**) Quantified fluorescence intensity (Fl. Int.) of accumulated nanoparticles from images and lysates of tumor-bearing mice ($n = 4$) after intravenous injection of Cy5-siRNA-cLPs and Cy5-siRNA-AuroLPs at 24 hours in terms of normalized Fl. Int. au, arbitrary units. (**B**) Percent injected dose (%ID) per gram tumor as measured above. (**C** to **K**) Reduction in tumor growth by intravenous injections of AuroLPs and cLPs containing MICU1-siRNA or CTL-siRNA-AuroLPs through the 12-day treatment period. Tumor size (C), representative images of tumor (D), tumor mass (E), MICU1 expression at protein and mRNA level with GAPDH as control (F and G), images and its quantification of MICU1 immunostained tumor (H), Ki67-stained (left) and TUNEL-stained (right) sections of tumors (I), the quantification of Ki67-stained proliferating cells (top), and TUNEL-stained apoptotic cells (bottom) (J) ($n = 6$). H&E-stained sections of tissues showing hepatitis in liver for MICU1-siRNA-cLPs (arrow head) (K). Scale bar, 50 μm. Data are expressed as means ± SD and were analyzed by using Student's *t* test (A and B) and one-way analysis of variance (ANOVA) followed by Dunnett's multiple comparisons test. a.u, arbitrary unit. $^{*}P \leq 0.05$, $^{**}P \leq 0.01$, $^{***}P \leq 0.001$, and $^{****}P \leq 0.000$. ns, not significant. Photo credit: M. N. Hossen (OUHSC).

complement cascade and (ii) the uptake of liposomes by the mononuclear phagocyte system in liver and spleen via opsonization (*13*). Accumulating evidence demonstrates that when injected systemically, cationic liposomes nonspecifically interact with blood cells, aggregate with serum proteins, and activate mechanisms for clearance of these foreign particles. This nonspecific interaction promotes toxicities such as hemolysis, liver damage, and inflammation in various compartments (e.g., blood, liver, spleen, lungs, etc.) (*6*, *23*). Although our cLPs are a cationic liposome, we did not observe major toxicities associated with intravenous injection of cLPs at a MICU1-siRNA dose of 0.2 μg/g body weight, as evidenced by no change in the body weight of mice throughout the duration of our therapeutic study (fig. S6, B and D). However, our histopathological analysis of liver and lungs exhibited minor toxicities probably due to highly cationic nature of MICU1-siRNA-cLPs at this dose as discussed above (Fig. 3K and fig. S6A). In contrast, AuroLPs have a small positive charge, which minimizes nonspecific interaction as discussed above, resulting in lack of toxicity. Thus, auroLPs enhance the gene silencing efficacy of siRNA with no appreciable toxicity in a preclinical animal model of ovarian cancer.

Antitumor efficacy of MICU1-siRNA-AuroLPs in a patient-derived xenograft model

The tumor microenvironment (TME) plays a critical role in tumor growth, metastasis, and therapy resistance; patient-derived xenograft (PDX) model tumor cells faithfully represent the original patient TME at the molecular level and thus offer unique opportunities to test the therapeutic efficacy of anticancer agents (*24*). As a prerequisite to using PDX models to assess our auroLPs, we first determined the expression of MICU1 in such models. We examined five PDX tumors; one, PDX-098, expressed moderately more MICU1 than the other four (Fig. 4A, top). PDX-098 was selected for further study because it grows faster in vivo than the others (fig. S7C). In addition, histopathological (H&E) analysis of PDX-098 revealed excessive activated fibroblast-like cells along with deposition of extracellular matrix in ovarian cancer patient–derived tissue, indicating an active TME and malignant potential (Fig. 4A, bottom). We implanted tissue subcutaneously in 80 nonobese diabetic (NOD)/severe combined immunodeficient (SCID) mice. When tumors attained ~100 mm^3, mice were randomly assigned to one of eight groups ($n = 10$ per group) for treatment; treatments were cLPs or auroLPs containing MICU1-siRNA at an siRNA dose of 0.2 mg/kg three times weekly with or without concomitant intraperitoneal injection of low-dose cisplatin (0.5 mg/kg twice a week). The treatment continued for 35 days (12 siRNA injections and 10 cisplatin injections). Control groups were phosphate-buffered saline (PBS), cisplatin alone, and control siRNA auroLPs with and without cisplatin. Animals were monitored for distress daily, and tumor size was measured weekly (Fig. 4B and fig. S7D). All animals were euthanized at completion; tumors, along with other organs, were excised; and size and weight were determined (Fig. 4, C to E). auroLPs significantly inhibited tumor growth, whereas inhibition of tumor growth by the cLPs was marginal. The auroLP/cisplatin combination completely inhibited tumor growth; the cLP/cisplatin combination reduced but did not eliminate tumor growth. Thus, silencing of MICU1 sensitizes PDX tumors to cisplatin. We determined MICU1 levels in tumor tissue lysates by immunoblot; MICU1 was reduced by treatment with auroLPs but not the other treatments (Fig. 4F). We also showed antitumor efficacy of AuroLPs by immunohistochemical and histopathological analysis in terms of decreasing proliferating cells (Ki67), increasing apoptotic cells (TUNEL), and reducing the amount of fibrosis/collagen fibers (such as activated fibroblast-like cells and collagen types I and III) (H&E and Sirius Red staining) (Fig. 4G). Body weights of animals did not vary significantly between groups and remained constant for the study duration, indicating the absence of toxicity (fig. S7E). In total, these data show that incorporation of low levels of AuNPs in a siRNA liposome formulation enhances its silencing efficacy both in vitro and in relevant preclinical animal models.

Mechanisms of enhanced silencing efficacy of auroliposomal formulations of siRNA

Having demonstrated the efficacy of our auroLP, we sought to elucidate the mechanisms underlying the nanoparticle-enhanced silencing by siRNA. One possibility is that auroLPs support siRNA stability in serum; however, as reported above, both auroLPs and cLPs prevent siRNA degradation in serum (Fig. 2F and fig. S8A). Alternatively, increased intracellular uptake may explain the phenomena; we monitored uptake by OV90 cancer cells of Cy5-labeled control siRNA delivered in various formulations. Fluorescence images indicated that uptake of cLPs and auroLPs was similar; uptake via other delivery systems, i.e., HF, direct AuNP conjugation, and free siRNA, was marginal (fig. S8B). Quantitative analysis showed that uptake from auroLPs (~30% of the dose) was almost twice that from cLPs (~18%); all other groups had uptake of ~4%. Thus, enhanced uptake of auroLPs may contribute to siRNA effectiveness (fig. S8C). It is not only the intracellular uptake, endosomal escape, and consequent avoidance of lysosomal degradation is another critical factor for siRNA efficacy; we interrogated endocytic uptake pathways for our liposomes. We used established inhibitors of the three main endocytosis pathways, namely, clathrin-mediated endocytosis (CME), caveolar-mediated endocytosis (CvME), and macropinocytosis and monitored uptake of liposomes containing Cy5-labeled control siRNA by OV90 cells (*25*). Uptake of cLPs was significantly inhibited by filipin (CvME; 52.8 ± 1.3%), brefeldin A (endocytosis; 34.7 ± 4.9%), and rottlerin (micropinocytosis; 35.4 ± 3.3%); only the CvME inhibitor filipin reduced auroLP uptake by ~83% (Fig. 5A and fig. S8D). The CME inhibitors chlorpromazine and chloroquine did not affect uptake of either liposome. These data suggest that incorporation of AuNP switches the endocytic pathway to be primarily via CvME. Caveolin-1 (CAV1) is both sufficient and necessary for the formation of morphologically defined caveolae (*26*); silencing CAV1 will inhibit CvME. To confirm the caveolar entry of auroLPs, we suppressed CAV1 in OV90 cells using CAV1 siRNA; CAV1 was ~75% reduced at 72 hours (Fig. 5B). In CAV1 knockdown cells, auroLP uptake decreased ~80%, while cLP uptake was only marginally affected (Fig. 5, C to E). We next assessed the impact of CAV1 knockdown on liposome-mediated silencing of MICU1. As expected, the silencing activity of MICU1-siRNA auroLPs was totally abrogated in CAV1 knockdown cells (Fig. 5F), confirming that auroLPs use the caveolar uptake pathway. Since they are below 200 nm in size and have slightly positive charge, nanoparticles are most likely to use CvME; caveolae have an average size of 60 to <200 nm (*25*, *26*, *27*–*28*).

Viral particles reportedly use CvME to avoid lysosomal degradation (*29*). Thus, we investigated the intracellular location of internalized particles and whether they colocalized with the lysosome. We used an endosomal antibody to label endosomes and LysoTraker Green to label lysosomes and monitored the intracellular location of liposomes containing Cy5-labeled control siRNA; the nucleus was stained with

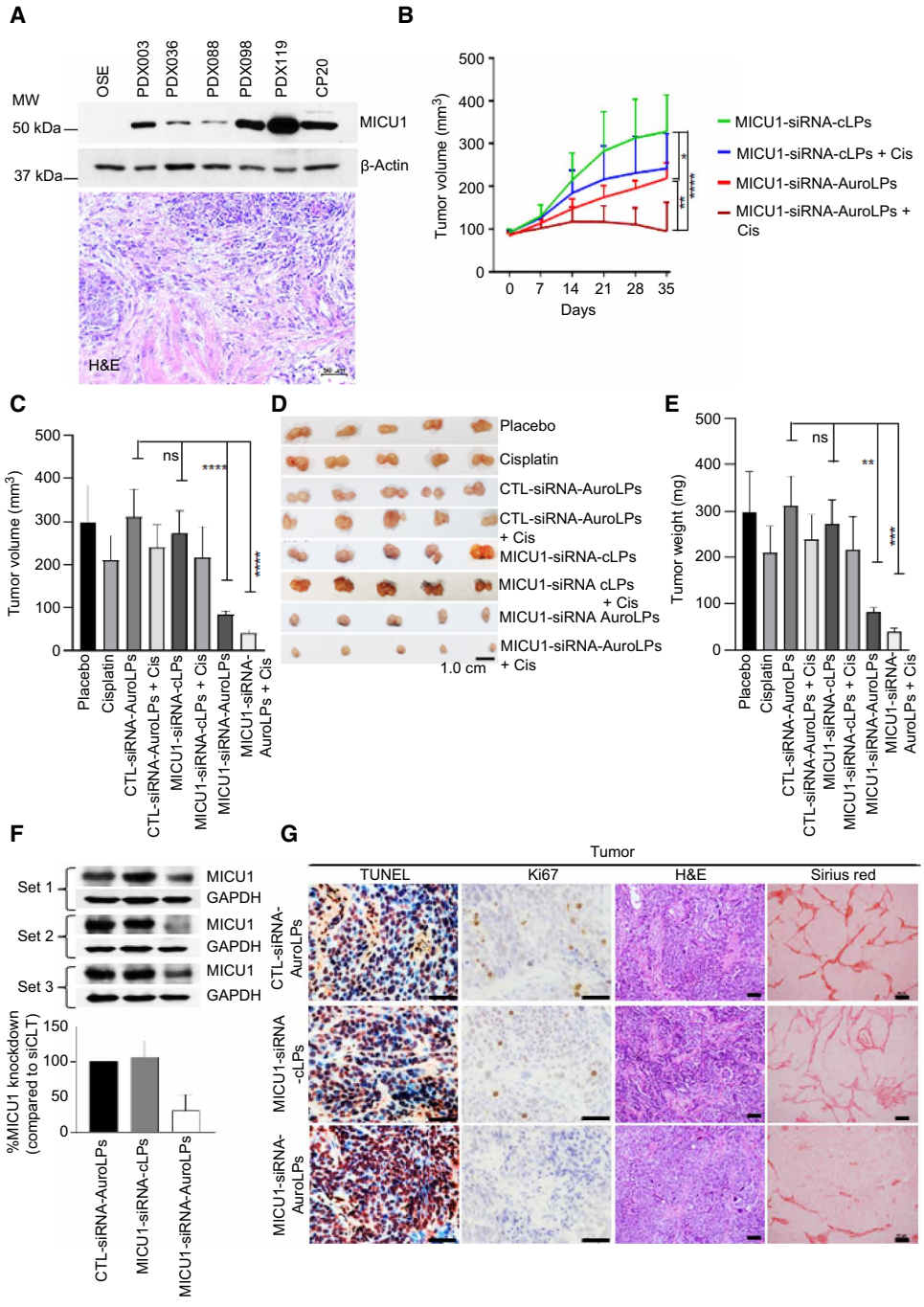

Fig. 4. Antitumor efficacy of MICU1-siRNA-AuroLPs PDX. (**A**) MICU1 protein expression in PDX models of primary high-grade serous ovarian cancer. MICU1 expression in different PDX tumors, compared to normal OSE and CP20 cells (top). Histopathological analysis of human ovarian tumor tissues by using H&E to confirm its tumorigenic characteristics (bottom). Scale bar, 50 μm. (**B** to **E**) Assessment of antitumor efficacy of auroLPs in PDX mice. PDX-098 was subcutaneously transplanted into NOD/SCID background mice ($n = 80$). Tumor-bearing PDX model mice (tumor size, 100 mm^3) were intravenously injected with cLPs and AuroLPs containing MICU1-siRNA (0.2 mg/kg/thrice weekly) or in combination with intraperitoneal injection of cisplatin (0.5 mg/kg/twice a week). The treatment was continued for 35 days. The tumor volume (tv) was measured weekly (B), and 35-day tv was shown separately (C). Representative tumor images (D) and tumor masses (E) were shown. (**F**) MICU1 expression in tumor lysates at 35 days with GAPDH as loading control. (**G**) The representative Ki67-, TUNEL-, H&E-, and Sirius red–stained sections of corresponding tumors. All statistical analyses were performed using one-way ANOVA followed by Dunnett's multiple comparisons test. *$P \leq 0.05$, **$P \leq 0.01$, ***$P \leq 0.001$, and ****$P \leq 0.0001$, $n = 5$ to 10. Photo credit: M. N. Hossen (OUHSC).

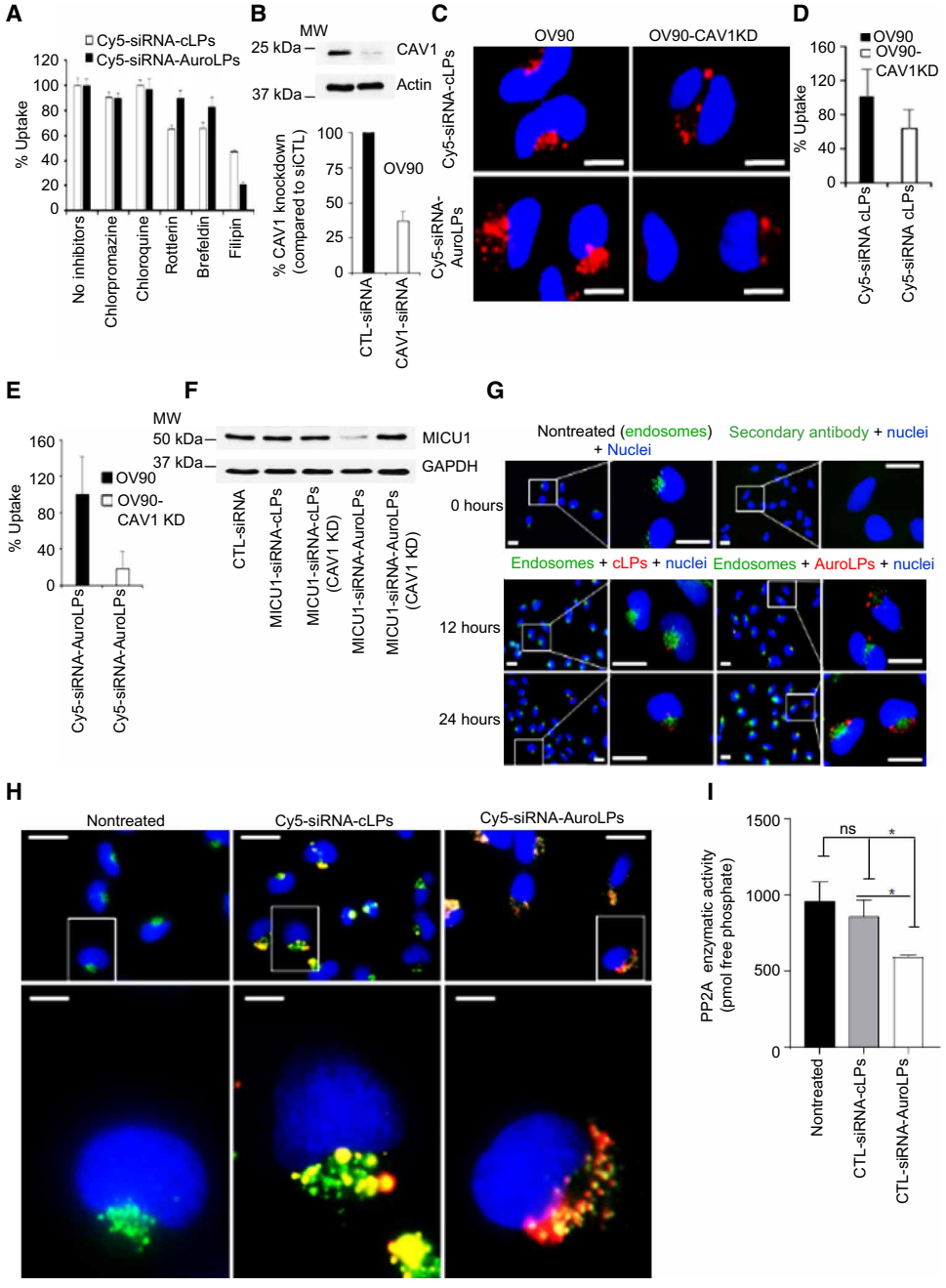

Fig. 5. Mechanisms of enhanced silencing efficacy of auroliposomal formulation of siRNA. (**A**) Evaluation of cellular uptake mechanisms of AuroLPs by pretreatment of OV90 cells with several chemical inhibitors for 2 hours followed by a further 4-hour incubation with Cy5-siRNA-cLPs and Cy5-siRNA-AuroLPs at 37°C. Data were represented as % uptake, means ± SD, $n = 3$. (**B** to **E**) Inhibition of cellular uptake of AuroLPs by CAV1 silencing. WB analysis showing expression of CAV1 after treatment of OV90 with CAV1-siRNA + RNAiMAX at 72 hours (B). The qualitative and quantitative uptake of Cy5-siRNA-AuroLPs and Cy5-siRNA-cLPs in CAV1 knockdown cells (OV90-CAV1KD) and OV90 (C to E). Scale bars, 10 μm. (**F**) WB of MICU1 protein in OV90 and OV90-CAV1KD after transfection with MICU1-siRNA-cLPs and MICU1-siRNA-AuroLPs for 72 hours. (**G** and **H**) Study of endosomal and lysosomal escape for Cy5-siRNA-cLPs, Cy5-siRNA-AuroLPs, and treated/nontreated cells for 12 and 24 hours. The endosomes (green), Cy5-siRNA (red), and nuclei (blue) were visualized under a fluorescence microscope (G). Observation of lysosomal colocalization (yellow) of above treatments at 24 hours (H). Scale bars, 10 and 5 μm. (**I**) Measurement of protein phosphatase 2A (PP2A) enzymes activity using immunoprecipitation with and/or without treating cells with CTL-siRNA-cLPs and CTL-siRNA-AuroLPs for 15 min. The statistical analysis was performed by one-way ANOVA followed by Dunnett's multiple comparisons test, means ± SD, $^*P < 0.05$, $n = 3$.

4′,6-diamidino-2-phenylindole (DAPI). auroLPs did not colocalize with endosomes, suggesting endosomal escape (Fig. 5G). In addition, most cLPs colocalized with the lysosome, indicating lysosomal degradation; in contrast, auroLPs did not colocalize with the lysosome, supporting our hypothesis that CvME uptake of auroLPs reduces lysosomal degradation and leads to enhanced gene silencing (Fig. 5H). To further investigate the mechanisms of switching of the uptake pathway, we assessed activity of the enzyme protein phosphatase 2A

(PP2A); PP2A regulates maturation of endosomes and their fusion with lysosomes (*29*). We measured enzymatic activity of PP2A using a commercially available kit (catalog no. 17-313, Millipore Sigma, Temecula, CA, USA). Treatment of OV90 cells with cLPs only marginally altered PP2A activity; however, auroLPs significantly reduced PP2A activity (~40%) (Fig. 5I). We measured PP2A activity in cells treated with 5-, 20-, and 50-nm auroLPs and Fe3O4-cLPs. As expected, treatment of ovarian cancer cells with 20-nm auroLPs significantly decreased PP2A activity (Fig. 5I), whereas other treatments had no effect (fig. S9). These results suggest that inhibition of PP2A activity is a critical factor in switching of the uptake pathway of auroLPs and the associated enhanced gene silencing activity. However, the mechanism of auroLP-mediated suppression of PP2A activity is unclear at this point and will be a focus of future investigations. As a whole, our data show that incorporation of a small nontherapeutic amount of AuNPs in a conventional siRNA-liposomal formulation switches its uptake to be predominantly via the caveolar uptake pathway, resulting in reduced lysosomal degradation and enhanced efficacy.

DISCUSSION

siRNA technology is an emerging platform for drug development; however, the lack of effective delivery systems has limited development of siRNA-based treatments. Here, we report a novel auroliposomal formulation for siRNA delivery that could extend the application of this technology clinically. Liposomes are attractive carriers for siRNA (*4*–*7*). The nanoscale dimension of liposomes means they can be combined with other nanoscale materials to form a so-called hybrid nanoparticle. These hybrid nanoparticles can execute multiple functions, for example, simultaneous therapeutic and diagnostic-imaging functions (*14*, *30*). Our auroLP is a new hybrid nanoparticle in which integration of 20-nm AuNPs in a conventional siRNA-liposomal formulation enhanced the silencing efficacy substantially. This effect was seen even with a dose of siRNA at which the silencing activity mediated by conventional cationic liposomes (cLPs) and commercially available transfection agents, including HF, Lipofectamine 3000, and RNA iMax is minimal (Fig. 2E). These results are consistent with the previously published data showing silencing of target genes (e.g., *MICU1* and *CBS*) within the dose range 50 to 200 nM depending on the cell type, type of siRNAs, and target genes and transfection reagents used *(12*, *21*, *31*–*33)*. Hybrid nanomaterials can yield not only the beneficial features of the individual components but also unique benefits arising from the combination *(14*, *30)*. For example, addition of AuNPs to liposomes may trigger the release of the liposome cargo upon exposure to UV light, increasing membrane fluidity and potentially killing cancer cells through photothermal therapy (*14*, *30*, *34*–*35*). Our report of AuNPs significantly increasing the efficacy of siRNA carried by liposomes is the first such finding in the literature.

Cationic liposomes are mainly used for the delivery of siRNA in vitro; however, the in vivo success rate remains low, possibly due to their rapid degradation and clearance by RES in the body (*8*, *9*, *15*). siRNA liposomes are taken up by cells through endocytosis pathways, including clathrin- and caveolae-mediated endocytosis as well as macropinocytosis (*36*); consistent with these previous reports, we found that cLPs are internalized by these multiple pathways. However, when we added 20-nm AuNPs to cLPs, we saw the uptake pathway shift to be predominantly via CvME. This shift in the uptake pathway allowed our auroLPs to escape the lysosome, thus avoiding degradation in turn allowing for enhanced silencing activity of the incorporated siRNA. Several viral particles (e.g., SV40) primarily use CvME as their entry route to bypass lysosomal degradation by inhibiting PP2A activity (*29*). Treatment of ovarian cancer cells with 20-nm AuroLPs significantly decreased the PP2A activity, whereas other treatments did not significantly alter PP2A activity level (fig. S9). Previously, we reported that among AuNPs of different sizes including 5, 10, 20, 50, and 100 nm, those of 20 nm had the highest efficacy in inhibiting functions of a number of heparin-binding growth factors and led to the inhibition of tumor growth and metastasis in orthotopic models of ovarian cancer (*15*). Similarly, among all the liposomes tested, only liposomes containing 20-nm AuNPs inhibited the function of PP2A. However, note here that the doses of AuNPs incorporated in auroLPs are well below their therapeutic doses. The charges of AuroLPs containing 5- and 50-nm AuNPs were comparable to that of cLPs (highly positive) (Fig. 1E and fig. S4). The inability of these particular liposomes to inhibit function of PP2A coupled with their highly positive charge indicates that they are taken up by multiple mechanisms such as micropinocytosis, CvME, and CME as shown for cLPs. Moreover, the slightly negative charge of Fe_3O_4-cLPs causes electrostatic repulsion from the plasma membrane as reported for negatively charged NPs and probably decreases their intracellular uptake (*6*, *7*), resulting in no effect on PP2A activity and hence decreased silencing efficacy. Thus, incorporation of AuNP of 20-nm size in cLPs plays two important roles: (i) By reducing overall charge, it switches intracellular uptake toward the caveolar uptake pathway and; (ii) by inhibiting PP2A activity, it further induces the caveolar uptake pathway and reduces lysosomal degradation by inhibiting fusion of the caveosome with the lysosome. Together, these phenomena result in increased uptake and gene silencing efficacy. Although the mechanism underlying auroLP-mediated suppression of PPA2 activity is unknown, many findings show that nonviral delivery systems have the potential to be taken up by cells via CvME depending on their size, surface charge, and surface modifications (*27*, *28*).

In addition to avoiding degradation, auroLPs may enhance siRNA activity via other mechanisms. For example, accumulation of carrier at the disease site is essential for drug delivery, and we demonstrated that auroLPs accumulate in tumor tissue at twice the rate of cLPs. Although the accumulation of both cLPs and auroLPs is mediated via the EPR effect (*22*), since neither are tethered to tumor targeting moieties, the high accumulation of auroLPs may result from the neutral charge being poorly recognized by the RES (*6*, *7*, *13*).

We assessed the efficacy of our auroLPs in two animal models: A human ovarian tumor cell line–derived xenograft and human ovarian PDX. We first demonstrated the antitumor efficacy of our auroliposomal formulation on human ovarian tumor cell line–derived xenograft mouse model. MICU1-siRNA auroLPs, compared to MICU1-siRNA-cLPs, significantly reduced tumor growth that was further confirmed through histopathological analysis and MICU1 gene silencing, in terms of mRNA and protein levels (Fig. 3). However, there is a variability in MICU1 knockdown within the tumors in MICU1-siRNA-cLP–treated animals (Fig. 3, F and G). There are three main reasons we believe contribute to the variability: (i) Accumulation of cLPs in tumors of cLP-treated animals is not equal, and there is a significant difference in uptake within the same treatment group. Figure 3 (A and B) shows that the amount of MICU1-siRNA delivered through cLPs is not the same across the tumors in this group,

resulting in differences in gene silencing efficacy. (ii) Lysosomal degradation of cLP—the uptake of cLPs into ovarian cancer cells is mediated via multiple mechanisms, and subsequently, the majority of the delivered siRNA is degraded in the lysosomal compartments (Fig. 5, H and I). Thus, the variability of uptake of cLPs among the tumors within the same group coupled with their lysosomal degradation results in the variable presence of functional siRNA leading to the variability in MICU1 gene silencing efficacy, which is further reflected

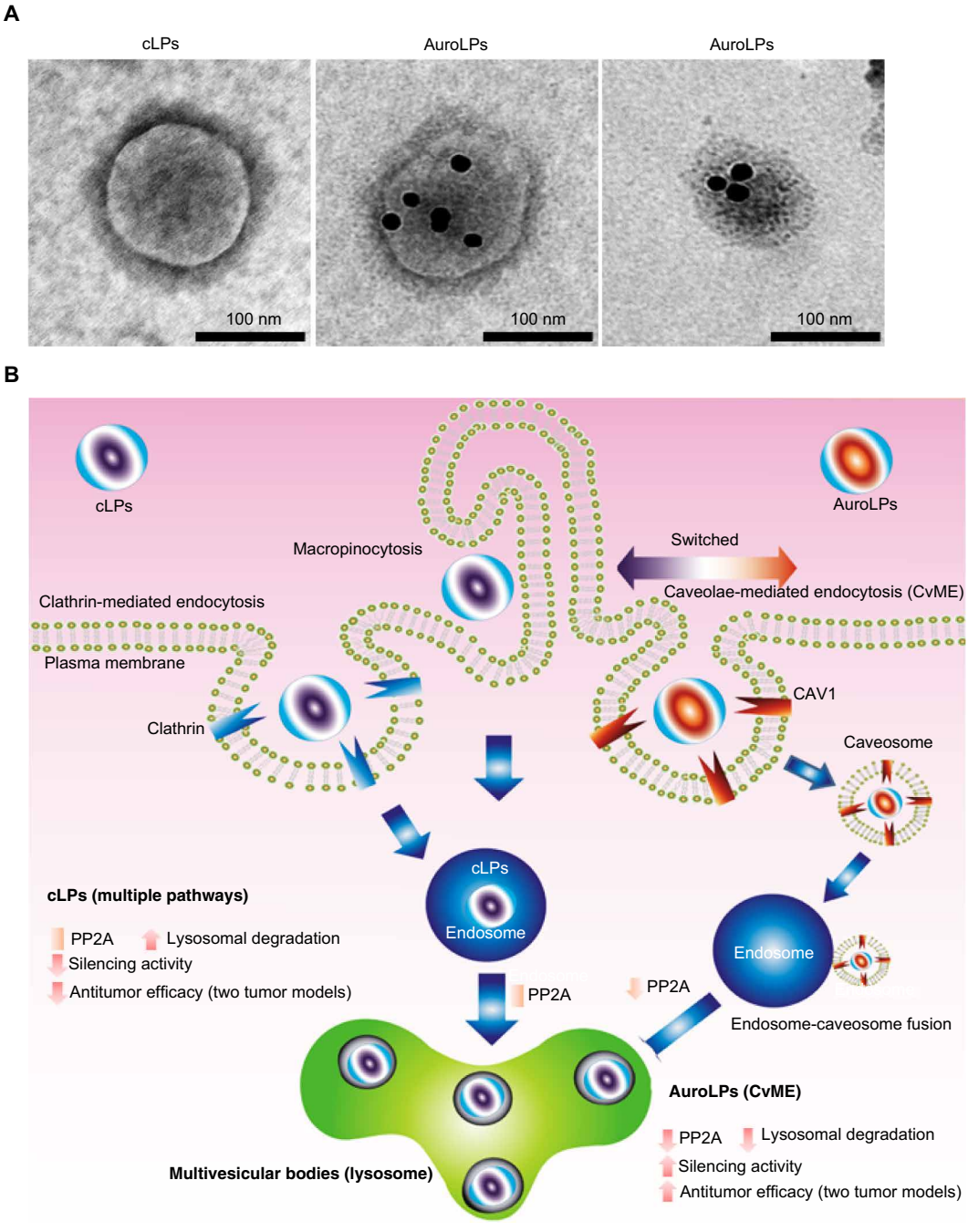

Fig. 6. Graphical illustration explaining enhanced gene silencing and antitumor activity of AuroLPs. (**A**) TEM micrographs of cLPs and auroliposomes (AuroLPs) stained with 0.2% uranyl acetate. Scale bar, 100 nm. (**B**) siRNA-cLPs was internalized into cancer cell using multiple pathways, including macropinocytosis, clathrin-, and caveolae-mediated endocytosis, whereas because of the addition of small amount of 20-nm AuNP into cLPs, the internalization route for AuroLPs was switched to mainly CvME. The concept of the switching of internalization pathway from multiple pathways to a single pathway was proved using three approaches: (i) evaluation of uptake in the presence of small chemical inhibitors, (ii) silencing of pathway-related target protein, and (iii) measuring the PP2A enzymatic activity. The resulting CvME pathway of uptake of AuroLPs resulted in several advantages including a decrease in lysosomal degradation due to a decrease in PP2A activity, enhanced silencing, and its corresponding antitumor efficacy in two ovarian tumor models.

in the downstream MICU1 protein levels. (iii) The inherent heterogeneity that exists in vivo is quite common, resulting in differential response within the group receiving identical treatments (*21*, *37*). PDX is a realistic TME model that maintains the original patient tumor (*24*). Thus, our MICU1-siRNA auroLPs were potent inhibitors of tumor growth in both models, and addition of a standard ovarian cancer treatment, cisplatin, boosted the inhibition even further in the PDX model.

In summary, we have developed a novel therapeutic delivery platform for siRNA by rational design and sorting of effective delivery systems. auroLPs provide a superior siRNA delivery system and were chosen by: (i) The sorting of conventional liposomal formulations through the modulation of structural lipid components and the ratio of lipids; and (ii) the optimization of size, shape, material, and ratio of the inorganic nanoparticle incorporated into the liposome. The resulting auroLPs exhibited excellent biostability, less lysosomal degradation, superior gene silencing, inhibition of clonal and tumor growth in human xenograft and PDX models of ovarian cancer, and lack of toxicity (Fig. 6). Although one liposomal siRNA drug is FDA-approved and others are in clinical trials (*8*–*11*), there is no siRNA therapeutic intervention for ovarian cancer. auroLPs provide a promising avenue for development of such a therapeutic, either alone or as combination therapy (e.g., cisplatin), that could translate to the clinic with potential applicability to multiple other malignancies.

MATERIALS AND METHODS

Chemicals and media

DOTAP (890890P), DOPE (850725P), DOPC (850375P), and PE-PEG (880120P) were purchased from Avanti Polar Lipids (Alabaster, Alabama, USA). Tetrachloroauric acid ($HAuCl_4 \cdot 3H_2O$) (520918) and sodium citrate tribasic trihydrate (S4641) were purchased from Sigma-Aldrich (St. Louis, MO, USA). Cell culture media RPMI 1640 (10-040-CV) was obtained from Corning Inc. (Corning, NY, USA). FBS (16000-044) and Penn-Strep (15140-122) were purchased from Life Technologies (Grand Island, NY, USA), Opti-MEM was from Thermo Fisher Scientific (Waltham, MA, USA). The scrambled control siRNA (cat. SIC001), siRNAs against human MICU1 (SASI_Hs01_00070249), CBS (SASI_Hs01_00214623), and CAV1 (SASI_Hs01_00199504) were procured from Sigma-Aldrich. The following primary antibodies were purchased from the specified vendor: rabbit monoclonal anti-MICU1 (#12524, Cell Signaling Technology, Danvers, MA, USA), rabbit polyclonal anti-CBS (#sc-67154, Santa Cruz Biotechnology, Dallas, TX, USA), anti-CAV1 (#SAB871521112, Sigma Aldrich), anti–glyceraldehyde-3-phosphate dehydrogenase (GAPDH) (Sigma-Aldrich), and anti-Ki67 (no. ab833, Abcam).

Nanoparticles

We synthesized 20-nm AuNPs as described previously (*38*). Spherical 5-nm AuNP (741949) and 50-nm AuNP (742007) and 25-nm GNR (900367) were purchased from Sigma-Aldrich. Twenty-nanometer Fe_3O_4 nanoparticles (IO-A20-5) were from Cytodiagnostics (Burlington, Ontario, Canada). Nanoparticles were characterized using UV-vis spectroscopy (SPECTROstar Nano, BMG Labtech), DLS, zeta potential measurements (Malvern Zetasizer Nano ZS), and TEM.

Preparation of cLPs and auroLPs

Liposomes were prepared using a common lipid film hydration method (*5*, *39*). Lipids (DOTAP, DOPE, and DOPC) (5 mg of each lipid) was dissolved in 1-ml *tert*-butanol at a final concentration of 5 mg/ml; PE-PEG_{2k} was dissolved in water. By modulating lipid compositions and ratio of lipids, 10 liposomes were designed; they were designated F1, F2, F3, F4, F5, F6, F7, F8, F9, and F10 and the structural lipid composition of each was respectively: DOTAP/DOPC (50:50); DOTAP/DOPE/DOPC (40:10:50); DOTAP/DOPE/DOPC (30:30:40); DOTAP/DOPE/DOPC/PE-PEG (30:10:40:20); DOTAP/DOPE/DOPC/PE-PEG (30:20:40:10); DOTAP/DOPE/DOPC/PE-PEG (30:25:40:05); DOTAP/DOPE (50:50); DOTAP/DOPE/PE-PEG [50:50:0.125 mole percent (mol %)]; DOTAP/DOPE/PE-PEG (50:50:0.25 mol %); and DOTAP/DOPE/PE-PEG (50:50:0.5 mol %). For siRNA liposomes, the specific siRNA was added at a ratio of 1:25 (w/w) siRNA: lipids (e.g., 10 μg of siRNA in 250 μg of lipid mixture). Tween 20 at a ratio of 1:18 (w/w) with respect to total lipids was added to all liposomes. All components were mixed in excess *tert*-butanol, and then, the mixture was dried overnight under vacuum in a lyophillizer. The dried film was hydrated by ribonuclease-free water containing either siRNA or siRNA-AuNP for 15 min, followed by vortexing (2 min), and the resulting liposomes were extruded using a polycarbonate membrane (pore size, 0.1 μm; cat. 610005, Avanti Polar Lipids, Alabaster, Alabama, USA). AuNPs, GNR, or Fe_3O_4 NPs containing siRNA liposomes were prepared by adding a mixture of AuNPs or GNR or Fe_3O_4 NPs and siRNA (10:1, w/w; e.g., 100 μg of AuNPs or GNR or Fe_3O_4NPs and 10 μg of siRNA) to the lipid mixture (e.g., total lipids of 250 μg) for the formulation (i.e., DOTAP:DOPE 50:50); liposomes containing AuNPs or GNR or Fe_3O_4 NPs only were prepared by adding only AuNPs or GNR or Fe_3O_4 NPs to the mixture. Particle size, polydispersity index, and zeta potentials for all formulations were determined using a Malvern Instruments Zetasizer. AuNP content was determined by INAA (*38*).

Determination of encapsulated and released siRNA

The encapsulated siRNA content of liposomes was determined using a RiboGreen assay kit (R11490, Invitrogen) according to the manufacturer's directions. A standard curve was prepared using known siRNA concentrations (i.e., 10, 5, 2.5, 1.25, 0.625, 0.312, and 0 μg/ml) and by measuring fluorescent intensity at λex = 485 nm and λem = 538 nm using a CLARIOstar plate reader (BMG Labtech, Ortenberg, Germany). Liposome formulations were centrifuged at 5000*g* for 30 to 40 min at 12°C in an Amicon Ultra 0.5-ml filter (MCW: 30 K), and the flowthrough and retained fractions were collected. The original liposome preparation, the flowthrough, and the retained fraction were all solubilized with 2% Triton X-100; the siRNA content of each was determined using RiboGreen by measuring fluorescence and comparison to the standard curve. The percentage encapsulation efficiency was calculated by subtraction of the flowthrough siRNA from the original total siRNA amount in incorporated.

Released siRNA was estimated as follows: Either siRNA-loaded liposomes (e.g., cLPs and AuroLPs) or siRNA-HF complex (500 μl) were placed into 0.5-ml Amicon filter tubes under an endo-lysosomal environment [i.e., acidic pH (5.0) with 10 mM GSH in nuclease-free PBS]. Tubes were incubated at 37°C with gentle shaking for 0.5, 1, 3, 6, 12, and 24 hours and then tubes were centrifuged at 5000*g* for 30 to 40 min at 12°C, and flowthrough fractions were collected. Flowthrough volumes were 0.45 ml, and at each time point, except 24 hours, 0.45 ml of fresh buffer was added to the tube. The siRNA amount in flowthrough fractions, collected at these time points, was determined by using RiboGreen assay, as previously described. The percentage release was calculated by subtraction as above; cumulative

release rate was calculated, determining percentage release of at various time points.

Imaging and quantification of AuNP

Nanoparticles and liposomes were visualized and imaged by TEM essentially, as previously described (*38*). Briefly, 300 Cu mesh formvar carbon–coated grid was hydrated by water, and a small drop of each nanoparticle (around 10 to 15 μl) was added to the grid, waited for 2 min, and removed the excess with a tissue paper by slightly touching the drop on the grid. Drop coating were repeated three times for each sample. After three repeats of drop coating, 0.2% uranyl acetate was added to the same grid and then left the grid overnight to air dry inside a chemical hood. The grid containing sample was then visualized under a Hitachi H7600 TEM at 80 kV equipped with a 2 k × 2 k.

Aggregation study of liposomal gold

The aggregation of AuNPs was performed in 150 mM NaCl, as previously described (*16*). Briefly, liposomal gold or AuNPs were treated with 150 mM NaCl for 10 to 15 min. The UV-vis spectra of the resulting solutions were determined (SPECTROstar Nano, BMG Labtech). TEM experiments were also performed for either liposomal gold or liposomal gold with NaCl, as previously discussed.

Cell lines, culture, and transfection

The epithelial ovarian cancer cell lines CP20, OV90, and OVCAR4 were routinely cultured in RPMI 1640 media containing 10% FBS and 1% penicillin-streptomycin at 37°C with 5% CO_2. For transfection, cells were cultured in 6-cm dishes containing 5×10^5 or 1.5×10^5 cells and transfected with specified reagents with either siRNAs or liposomes according to the manufacturer's protocols. Transfection reagents used were HF (Qiagen, CA, USA), Lipofectamine 3000 (Thermo Fisher Scientific), and Lipofectamine RNAiMax (Thermo Fisher Scientific).

FBS digestion assay

FBS digestion of samples, including free siRNA, siRNA-cLPs, siRNA-AuroLPs, siRNA + AuNP, and siRNA + HF, was performed using 100% FBS (1:1, v/v) in a total volume of 40 μl at 37°C for 15 min or 24, 48, 72, and 96 hours at 37°C with gentle shaking. Digestion was assessed by gel electrophoresis (1.5% agarose) of 20-μl aliquots of the reaction (equivalent to 1 or 1.5 μg of siRNA) in the presence of tris-borate EDTA buffer.

Cellular uptake and enzymatic assays

CP20 or OV90 cells (at a density of 5×10^4 per well in a 24-well plate) were cultured overnight on coverslips and were treated with Cy5 CTL-siRNA, Cy5 CTL-siRNA-cLPs, Cy5 CTL-siRNA-AuroLPs, conjugate (20-nm AuNP-cy5 CTL-siRNA), and complex (HF+cy5 siRNA) at a dose of 25 nM Cy5 siRNA. At various time points (2, 5, 24, and 48 hours), cells were fixed with 4% paraformaldehyde (PFA), nuclei were stained with DAPI and were then visualized by fluorescence microscopy (Carl Zeiss Axioplan, Germany). To evaluate the mechanism of cellular uptake, cultured cells were incubated for 2 hours in the presence or absence of the following chemical inhibitors: chlorpromazine (10 μg/ml), 10 μM chloroquine, filipin (5 μg/ml), 10 μM rottlerin, or 5 μM brefeldin. After the 2-hour incubation, Cy5 CTL-siRNA-cLPs and cy5 CTL-siRNA-AuroLPs at a dose of 25 nM CTL Cy5 siRNA were added for a further 4 hours. These cells were processed as described previously and were then visualized by fluorescence microscopy (Carl Zeiss Axioplan, Germany). For the quantitative determination of uptake, cells were grown in 24-well plates without coverslips and were incubated with the same groups, as mentioned above at a final concentration of 25 nM Cy5 siRNA for 30 min, 1, 3, 6, 12, and 24 hours. Cells were lysed after these periods with radioimmunoprecipitation assay (RIPA) cell lysis buffer, collected the supernatants after a brief centrifugation, and were quantified the fluorescence intensity at λex/λem = 650/670 nm using a CLARIOstar plate reader (BMG Labtech, Ortenberg, Germany). For quantitative evaluation of the mechanism of cellular uptake of AuroLPs in the presence of small inhibitors, cells were prepared and processed, as described above. The percentage uptake was determined by using the following formulae: % uptake = (measured fl. int. of sample with inhibitor/measured fl. int. of sample without inhibitor) × 100. For the observation of uptake in CAV1 knockdown cells, knockdown cells were prepared by the treatment of CAV1 siRNA at a dose of 133 nM CAV1 siRNA and were then treated with 25 nM Cy5 CTL-siRNA-cLPs or Cy5 CTL-siRNA-AuroLPs. After 4 hours, cells were processed, as described previously. For endosomal and lysosomal escape studies, cells were prepared as described previously and were treated with 25 nM Cy5 CTL-siRNA-cLPs or Cy5 CTL-siRNA-AuroLPs. At various time points (0, 12, and 24 hours), cells were washed with PBS, fixed with 4% PFA for 15 min, treated with 0.1% Triton X-100, washed three times, blocked with 5% bovine serum albumin (BSA) for 30 min, and incubated with EEA1 rabbit primary antibody (2411S, CST) overnight, following incubation with the Alexa 488 secondary antibody and additional washing cells were stained with LysoTracker green (Invitrogen), washed, and fixed. The nuclei of these cells were stained with DAPI and were then visualized by fluorescence microscopy (Carl Zeiss Axioplan, Germany).

Immunoblotting

For immunoblotting, cells were lysed using RIPA buffer supplemented with proteinase inhibitor (Pierce, Appleton, WI, USA) (1:100, v/v); cells were lysed ice for 30 min with vortexing every 5 min. After centrifugation at 10,000*g* for 15 min, supernatants were collected. Cell lysates were incubated at 100°C for 10 min in Laemmli buffer containing β-mercaptoethanol, and the denatured cell lysates were separated on 10% tris-glycine SDS–polyacrylamide gel electrophoresis gels before transfer to polyvinylidene difluoride membranes. Membranes were blocked using 5% BSA for 30 min at room temperature before incubation with primary antibody in 5% BSA overnight at 4°C. Primary antibodies were rabbit anti-MICU1 (1:1000), rabbit anti-CBS (1:1000), rabbit anti-CAV1 (1:1000), rabbit anti-GAPDH, and rabbit anti-actin (1:10000). Following three washes with TBST (Tris Buffered Saline with Tween20), membranes were incubated with secondary antibody at a concentration of 1:10,000 for 2 hours at room temperature before development with appropriate reagents. Developed immunoblots were scanned, and the intensity of bands was quantified with ImageJ (image processing and analysis in Java, National Institutes of Health), where GAPDH was used for normalization. Excised tumor tissues were sliced into small pieces, incubated in RIPA containing protease inhibitor, and homogenized. Undigested debris was then removed by centrifugation, and the supernatant was processed for immunoblotting as above.

Isolation of RNA and analysis of mRNA expression using qRT-PCR

Total RNA was extracted from cells or sonicated tumor tissue using Quick-RNA Plus (Zymo Research, Irvine, CA, USA) according to the

manufacturer's protocols. Isolated RNA was retrotranscribed in a 20-μl reverse transcription reaction using a iScript cDNA synthesis kit (Bio- Rad, Hercules, CA, USA) as directed by the manufacturer. Synthesized cDNA was used for quantitative real-time polymerase chain reaction (qRT-PCR) using iTaq SYBR Green (Bio-Rad) following the supplier's protocols. The relative abundance of mRNA, using GAPDH as an internal control, was calculated by using the comparative cycle threshold method ($2^{\wedge}$-ΔΔCT) (*21*). Primer sequences were as follows: MICU1: 5′-GAGGCAGCTCAAGAAGCACT-3′ (forward) and MICU1:5′-CAAACACCACATCACACACG-3′ (reverse); GAPDH: 5′-CACCATCTTCCAGGAGCGAG-3′ (forward) and GAPDH: 5′-CCTTCTCCATGGTGGTGAAGAC-3′ (reverse).

Cell viability and clonal growth assays

Cells were grown in 96-well plates at a density of 3000 cells per well overnight and then treated with specified siRNA preparations. After 48 hours, cell viability was assessed using the MTT (3-(4,5-dimethylthiazol-2-yl)-2,5-diphenyl tetrazolium bromide) assay (Cell Proliferation Kit I, Sigma-Aldrich) according to the manufacturer's protocol. For clonal growth assays, cells were seeded at a density of 200 cells per well in six-well plates and were cotransfected with the specified treatments. After 8 to 12 days, colonies were stained with crystal violet, dried, imaged, and counted using the GelCount (Oxford Optronix).

Animal studies

Female athymic nude mice (NCr-nu/nu; 5 to 6 weeks old) were purchased from Charles River (Delaware, Newark, USA). All mice were kept under specific pathogen-free conditions in facilities that were approved by the American Association for Accreditation of Laboratory Animal Care and in accordance with all current regulations and standards of the U.S. Department of Agriculture, U.S. Department of Health and Human Services, and National Institutes of Health. The protocol was approved by the University of Oklahoma Health Sciences Center (OUHSC) Institutional Animal Care and Use Committee (IACUC).

OV90 cells (2×10^7) in 100-μl PBS were subcutaneously injected into a total of 15 mice. When tumor size reached 100 μm, the mice were randomly assigned to three groups ($n = 5$ per group). Groups then received one of three treatments by intravenous injection every 4 days; treatments were 0.2 mg/kg of control siRNA in auroLPs, MICU1-siRNA in cLPs, or MICU1-siRNA in auroLPs. Treatment continued for 12 days at which point control mice had reached IACUC-mandated endpoints. Individual tumors were measured using a vernier caliper every 2 days, and tumor volume was calculated using the following: tumor volume (mm^3) = length × ($width^2$)/2. Body weights were also recorded every 2 days. After 12 days, animals were euthanized, and tumors and other tissues were excised for downstream analyses; images of tumor tissues were captured by digital camera, and tumor masses were determined.

Additional animal procedures involving NOD/SCID mice were performed by the Patient-Derived Xenograft and Preclinical Therapeutics (PDX-PCT) Core facility at the Oklahoma Medical Research Foundation (OMRF) and approved by the OMRF's IACUC. NOD/SCID (stock no. 001303) mice were purchased from the Jackson Laboratory (Bar Harbor, ME). PDXs used for this study were developed by the PDX-PCT core facility. PDXs were generated from high-grade serous ovarian tumors from patients of Stephenson Cancer Center at OUHSC; patients gave informed consent under a protocol approved by the OUHSC Institutional Review Board. Animals were subcutaneously implanted into the left flank with viable PDX fragment using routine procedures (*40*). Briefly, the mouse was anesthetized with isoflurane. The surgical site on left flank was cleared from hairs using an electric shaver. A providone-iodine swabstick was used to sterilize the surgical area, followed by washing off a providone-iodine with 70% ethanol. A 5-mm incision was made on the left flank with scissors. One tumor fragment of around 3 mm^3 was inserted subcutaneously into the flank. Skin incision was closed with one wound clip. Wound clip was removed 10 days after surgery. After the tumor volume reached approximately 100 mm^3 in 35 to 49 days, mice were randomized. Mice were monitored weekly for development and progression of tumor and symptoms of physical distress or illness; body weights were also recorded weekly. Mice with established tumors of approximately 100-mm^3 volume were randomized and treated as specified. Tumor dimensions were measured with vernier caliper, and tumor volumes were calculated as above. Mice were treated for 5 weeks. Mice showing reaching IACUC defined endpoints were euthanized by CO_2 inhalation and necropsied. Upon completion of the experiment, tumors were from all mice were collected and snap-frozen in liquid nitrogen or fixed for downstream analyses. Pharmaceutical grade cisplatin (Alvogen) for PDX experiments was purchased from the OUHSC Pharmacy. Cisplatin was dissolved in saline at 0.5 mg/ml.

Biodistribution

Athymic nude mice having tumors size of 500 μm were injected with either 5 μg of Cy5-labeled liposomes. Twenty-four hours later, tissues (tumor, liver, spleen, kidneys, lungs, and heart) were imaged by using Carestream Xtreme In Vivo Imaging System, and the fluorescent intensity was quantified. To identify the percentage of injected dose accumulating at specific sites, tissues were collected and weighed, they were then cut into small pieces and lysed by homogenizing in 500-μl RIPA lysis buffer, and the samples were centrifuged to remove undigested debris. The fluorescence intensity of the supernatants was then measured, and percentage of the dose accumulating was calculated by subtraction from values derived from fluorescence intensity of total injected dose (5 μg) added to tissue lysate from untreated animals.

Immunohistochemistry

Mouse tissues were fixed in 10% formalin, embedded in paraffin, and sectioned (4 μm) using a Leica multistainer (ST5020) using standard protocols. Briefly, tissue sections were deparaffinized in sequential treatments in 100% xylene, 100% ethanol, and 100% water and were then stained with H&E, Sirius Red or Ki67, MICU1, or TUNEL. For staining with Ki67 and MICU1, antigen retrieval was obtained by heating the deparaffinized tissue sections in citrate buffer (pH 6) for 10 min at 95°C. Sections were then blocked with protein block and stained with the following antibodies at the specified titers overnight at 4°C: Ki67 (1:50) and MICU1 (1:50). The ABC system (Vector) was used to detect the protein according to the manufacturer's protocol. For TUNEL staining, the deparaffinized tissue sections were incubated with the In situ Cell Death Detection Kit, AP (Roche Diagnostics GmbH, Manheim, Germany) according to the manufacturers' protocol. For Sirius red (cat. ab150681, Abcam) staining, the deparaffinized tissue sections were stained according to the manufacturers' protocol. Images were captured by using Nikon Eclipse Ni microscope.

Statistics

All results are derived from at least three individual experiments, unless stated otherwise, and are reported as means ± SD. The statistical significance of differences between groups was determined using unpaired Student's *t* test and one-way analysis of variance (ANOVA) followed by multiple comparisons test via Prism Pad software. Significant *P* values are indicated in figures and/or legends as $*P \leq 0.05$, $**P \leq 0.01$, $***P \leq 0.001$, and $****P \leq 0.0001$.

SUPPLEMENTARY MATERIALS

Supplementary material for this article is available at http://advances.sciencemag.org/cgi/content/full/6/30/eaba5379/DC1

REFERENCES AND NOTES

1. A. Fire, S. Xu, M. K. Montgomery, S. A. Kostas, S. E. Driver, C. C. Mello, Potent and specific genetic interference by double-stranded RNA in *Caenorhabditis elegans*. *Nature* **391**, 806–811 (1998).
2. A. P. McCaffrey, L. Meuse, T.-T. T. Pham, D. S. Conklin, G. J. Hannon, M. A. Kay, Gene expression: RNA interference in adult mice. *Nature* **418**, 38–39 (2002).
3. R. Kanasty, J. R. Dorkin, A. Vegas, D. Anderson, Delivery materials for siRNA therapeutics. *Nat. Mater.* **12**, 967–977 (2013).
4. Y. Zhao, L. Huang, Lipid nanoparticles for gene delivery. *Adv. Genet.* **88**, 13–36 (2014).
5. C. N. Landen Jr., A. Chavez-Reyes, C. Bucana, R. Schmandt, M. T. Deavers, G. Lopez-Berestein, A. K. Sood, Therapeutic *EphA2* gene targeting *in vivo* using neutral liposomal small interfering RNA delivery. *Cancer Res.* **65**, 6910–6918 (2005).
6. Y. Xia, J. Tian, X. Chen, Effect of surface properties on liposomal siRNA delivery. *Biomaterials* **79**, 56–68 (2016).
7. V. P. Torchilin, Recent advances with liposomes as pharmaceutical carriers. *Nat. Rev. Drug Discov.* **4**, 145–160 (2005).
8. R. Solomon, A. A. Gabizon, Clinical pharmacology of liposomal anthracyclines: Focus on pegylated liposomal doxorubicin. *Clin. Lymphoma Myelom* **8**, 21–32 (2008).
9. A. Wang-Gillam, C. P. Li, G. Bodoky, A. Dean, Y.-S. Shan, G. Jameson, T. Macarulla, K.-H. Lee, D. Cunningham, J. F. Blanc, R. A. Hubner, C.-F. Chiu, G. Schwartsmann, J. T. Siveke, F. Braiteh, V. Moyo, B. Belanger, N. Dhindsa, E. Bayever, D. D. Von Hoff, L.-T. Chen; NAPOLI-1 Study Group, Nanoliposomal irinotecan with fluorouracil and folinic acid in metastatic pancreatic cancer after previous gemcitabine-based therapy (NAPOLI-1): A global, randomised, open label, phase 3 trial. *Lancet* **387**, 536–536 (2016).
10. U. Bulbake, S. Doppalapudi, N. Kommineni, W. Khan, Liposomal formulations in clinical use: An updated review. *Pharmaceutics* **9**, 12 (2017).
11. H. Ledford, Gene-silencing technology gets first drug approval after 20-year wait. *Nature* **560**, 291–292 (2018).
12. S. Bhattacharyya, S. Saha, K. Giri, I. R. Lanza, K. S. Nair, N. B. Jennings, C. Rodriguez-Aguayo, G. Lopez-Berestein, E. Basal, A. L. Weaver, D. W. Visscher, W. Cliby, A. K. Sood, R. Bhattacharya, P. Mukherjee, Cystathionine beta-synthase (CBS) contributes to advanced ovarian cancer progression and drug resistance. *PLOS ONE* **8**, e79167 (2013).
13. T. Ishida, H. Harashima, H. Kiwada, Liposome clearance. *Biosci. Rep.* **22**, 197–224 (2002).
14. W.-K. Rhim, J.-S. Kim, J.-M. Nam, Lipid–gold-nanoparticle hybrid-based gene delivery. *Small* **4**, 1651–1655 (2008).
15. R. R. Arvizo, S. Saha, E. Wang, J. D. Robertson, R. Bhattacharya, P. Mukherjee, Inhibition of tumor growth and metastasis by a self-therapeutic nanoparticle. *Proc. Natl. Acad. Sci. U.S.A.* **110**, 6700–6705 (2013).
16. C. K. Elechalawar, M. N. Hossen, P. Shankarappa, C. J. Peer, W. D. Figg, J. D. Robertson, R. Bhattacharya, P. Mukherjee, Targeting pancreatic cancer cells and stellate cells using designer nanotherapeutics in vitro. *Int. J. Nanomedicine* **15**, 991–1003 (2020).
17. L. Zhao, D. Jiang, Y. Cai, X. Ji, R. Xie, W. Yang, Tuning the size of gold nanoparticles in the citrate reduction by chloride ions. *Nanoscale* **4**, 5071–5076 (2012).
18. K. Sugikawa, K. Matsuo, A. Ikeda, Suppression of gold nanoparticle aggregation on lipid membranes using nanosized liposomes to increase steric hindrance. *Langmuir* **35**, 229–236 (2019).
19. P. R. Cullis, M. J. Hope, Lipid nanoparticle systems for enabling gene therapies. *Mol. Ther.* **25**, 1467–1475 (2017).
20. J. Gilleron, W. Querbes, A. Zeigerer, A. Borodovsky, G. Marsico, U. Schubert, K. Manygoats, S. Seifert, C. Andree, M. Stöter, H. Epstein-Barash, L. Zhang, V. Koteliansky, K. Fitzgerald, E. Fava, M. Bickle, Y. Kalaidzidis, A. Akinc, M. Maier, M. Zerial, Image-based analysis of lipid nanoparticle-mediated siRNA delivery, intracellular trafficking and endosomal escape. *Nat. Biotechnol.* **31**, 638–646 (2013).
21. P. K. Chakraborty, S. B. Mustafi, X. Xiong, S. K. D. Dwivedi, V. Nesin, S. Saha, M. Zhang, D. Dhanasekaran, M. Jayaraman, R. Mannel, K. Moore, S. M. Meekin, D. Yang, R. Zuna, K. Ding, L. Tsiokas, R. Bhattacharya, P. Mukherjee, MICU1 drives glycolysis and chemoresistance in ovarian cancer. *Nat. Commun.* **8**, 14634 (2017).
22. H. Maeda, H. Nakamura, J. Fang, The EPR effect for macromolecular drug delivery to solid tumors: Improvement of tumor uptake, lowering of systemic toxicity, and distinct tumor imaging in vivo. *Adv. Drug Deliv. Rev.* **65**, 71–79 (2013).
23. H. Li, Y. Chen, Y. Deng, Y. Wang, X. Ke, T. Ci, Effects of surface charge of low molecular weight heparin-modified cationic liposomes on drug efficacy and toxicity. *Drug Dev. Ind. Pharm.* **43**, 1163–1172 (2017).
24. Y. Lai, X. Wei, S. Lin, L. Qin, L. Cheng, P. Li, Current status and perspectives of patient-derived xenograft models in cancer research. *J. Hematol. Oncol.* **10**, 106 (2017).
25. J. Conde, N. Oliva, M. Atilano, H. S. Song, N. Artzi, Self-assembled RNA-triple-helix hydrogel scaffold for microRNA modulation in the tumour microenvironment. *Nat. Mater.* **15**, 353–363 (2016).
26. N. Ariotti, J. Rae, N. Leneva, C. Ferguson, D. Loo, S. Okano, M. M. Hill, P. Walser, B. M. Collins, R. G. Parton, Molecular characterization of caveolin-induced membrane curvature. *J. Biol. Chem.* **290**, 24875–24890 (2015).
27. J. H. Kang, W. Y. Jang, Y. T. Ko, The effect of surface charges on the cellular uptake of liposomes investigated by live cell imaging. *Pharm. Res.* **34**, 704–717 (2017).
28. S. N. Xiang, H. Tong, Q. Shi, J. C. Fernandes, T. Jin, K. Dai, X. Zhang, Uptake mechanisms of non-viral gene delivery. *J. Control. Release* **158**, 371–378 (2012).
29. A. L. Kiss, E. Botos, Endocytosis *via* caveolae: Alternative pathway with distinct cellular compartments to avoid lysosomal degradation? *J. Cell. Mol. Med.* **13**, 1228–1237 (2009).
30. M. J. Sailor, J.-H. Park, Hybrid nanoparticles for detection and treatment of cancer. *Adv. Mater.* **24**, 3779–3802 (2012).
31. K. Mallilankaraman, P. Doonan, C. Cárdenas, H. C. Chandramoorthy, M. Müller, R. Miller, N. E. Hoffman, R. K. Gandhirajan, J. Molgó, M. J. Birnbaum, B. S. Rothberg, D.-O. D. Mak, J. K. Foskett, M. Madesh, MICU1 is an essential gatekeeper for MCU-mediated mitochondrial Ca^{2+} uptake that regulates cell survival. *Cell* **151**, 630–644 (2012).
32. J. Yan, F. Teng, W. Chen, Y. Ji, Z. Gu, Cystathionine β-synthase-derived hydrogen sulfide regulates lipopolysaccharide-induced apoptosis of the BRL rat hepatic cell line in vitro. *Exp. Ther. Med.* **4**, 832–838 (2012).
33. S. Saha, P. K. Chakraborty, X. Xiong, S. K. D. Dwivedi, S. B. Mustafi, N. R. Leigh, R. Ramchandran, P. Mukherjee, R. Bhattacharya, Cystathionine β-synthase regulates endothelial function *via* protein *S*-sulfhydration. *FASEB J.* **30**, 441–456 (2016).
34. S.-H. Park, S.-G. Oh, J.-Y. Mun, S.-S. Han, Loading of gold nanoparticles inside the DPPC bilayers of liposome and their effects on membrane fluidities. *Colloids Surf. B Biointerfaces* **48**, 112–118 (2006).
35. A. K. Rengan, A. B. Bukhari, A. Pradhan, R. Malhotra, R. Banerjee, R. Srivastava, A. De, In vivo analysis of biodegradable liposome gold nanoparticles as efficient agents for photothermal therapy of cancer. *Nano Lett.* **15**, 842–848 (2015).
36. A. Alshehri, A. Grabowska, S. Stolnik, Pathways of cellular internalisation of liposomes delivered siRNA and effects on siRNA engagement with target mRNA and silencing in cancer cells. *Sci Rep.* **8**, 3748 (2018).
37. C. M. Roberts, C. Cardenas, R. Tedja, The role of intra-tumoral heterogeneity and its clinical relevance in epithelial ovarian cancer recurrence and metastasis. *Cancer* **11**, 1083 (2019).
38. M. N. Hossen, G. Rao, A. Dey, J. D. Robertson, R. Bhattacharya, P. Mukherjee, Gold nanoparticle transforms activated cancer -associated fibroblasts to quiescence. *Acs Appl. Mater. Interfaces* **11**, 26060–26068 (2019).
39. M. N. Hossen, K. Kajimoto, R. Tatsumi, M. Hyodo, H. Harashima, Comparative assessments of crucial factors for a functional ligand-targeted nanocarrier. *J. Drug Target.* **22**, 600–609 (2014).
40. M. Bieniasz, P. Radhakrishnan, N. Faham, J.-P. De La O, A. L. Welm, Preclinical efficacy of ron kinase inhibitors alone and in combination with PI3K inhibitors for treatment of sfRon-expressing breast cancer patient-derived xenografts. *Clin. Cancer Res.* **21**, 5588–5600 (2015).

Acknowledgment: We thank all who were involved in discussions and planning as well as those who helped in performing experiments. **Funding:** This work was supported by CA213278, CA136494, and P30 CA225500 Team Science grants. Preparation of this publication was supported in part by the National Cancer Institute Cancer Center Support Grant P30CA225500 awarded to the University of Oklahoma Stephenson Cancer Center; Services from the Office of Cancer Research were used. We also thank the Peggy and Charles Stephenson Cancer Center at the University of Oklahoma Health Sciences Center for a seed grant and an Institutional Development Award (IDeA) from the National Institute of General Medical Sciences of the NIH under grant no. P20 GM103639 for the use of Histology and Immunohistochemistry Core, which provided immunohistochemistry and image analysis service. **Author contributions:** P.M. supervised the project. P.M. and M.N.H. conceived of the project, designed the study, and wrote the manuscript. M.N.H. performed the experiments and data analysis. L.W. and M.N.H. prepared PDX model mice and performed the therapeutic study on this model under the guidance of P.M. and M.B. M.N.H. and H.R.C. performed stability

testing of nanoparticles. J.D.R. measured the gold content of nanoparticles. K.-M.F. evaluated the IHC sections for functional and toxic effects of nanoparticles. S.W. helped in TEM. R.B. helped conduct experiments (microscopy) and was involved in all discussions. All authors reviewed the manuscript. **Competing interests:** P.M., M.N.H., and R.B. are authors on a patent application (no. 20190255088, filed 15 February 2019). The authors declare that they have no other competing interests. **Data and materials availability:** All data needed to evaluate the conclusions in the paper are present in the paper and/or the Supplementary Materials. Additional data related to this paper may be requested from the authors.

Submitted 11 December 2019
Accepted 9 June 2020
Published 22 July 2020
10.1126/sciadv.aba5379

Citation: M. N. Hossen, L. Wang, H. R. Chinthalapally, J. D. Robertson, K.-M. Fung, S. Wilhelm, M. Bieniasz, R. Bhattacharya, P. Mukherjee, Switching the intracellular pathway and enhancing the therapeutic efficacy of small interfering RNA by auroliposome. *Sci. Adv.* **6**, eaba5379 (2020).